



Comparison of different reconstruction algorithms for three-dimensional ultrasound imaging in a neurosurgical setting

D. Miller^{1*}
 C. Lippert²
 F. Vollmer³
 O. Bozinov⁴
 L. Benes⁵
 D.M. Schulte¹
 U. Sure¹

¹Department of Neurosurgery,
University Hospital Essen

²University of Applied Sciences
Giessen-Friedberg

³Brainlab AG

⁴Department of Neurosurgery,
University Hospital Zurich

⁵Department of Neurosurgery,
University Hospital Marburg

*Correspondence to: Dr Dorothea Miller, Department of Neurosurgery, University Hospital Essen, Hufelandstr. 55, 45147 Essen, Germany.
E-mail: dorothea.miller@uk-essen.de

Abstract

Background Freehand three-dimensional ultrasound imaging (3D-US) is increasingly used in image-guided surgery. During image acquisition, a set of B-scans is acquired that is distributed in a non-parallel manner over the area of interest. Reconstructing these images into a regular array allows 3D visualization. However, the reconstruction process may introduce artefacts and may therefore reduce image quality. The aim of the study is to compare different algorithms with respect to image quality and diagnostic value for image guidance in neurosurgery.

Methods 3D-US data sets were acquired during surgery of various intracerebral lesions using an integrated ultrasound-navigation device. They were stored for post-hoc evaluation. Five different reconstruction algorithms, a standard multiplanar reconstruction with interpolation (MPR), a pixel nearest neighbour method (PNN), a voxel nearest neighbour method (VNN) and two voxel based distance-weighted algorithms (VNN2 and DW) were tested with respect to image quality and artefact formation. The capability of the algorithm to fill gaps within the sample volume was investigated and a clinical evaluation with respect to the diagnostic value of the reconstructed images was performed.

Results MPR was significantly worse than the other algorithms in filling gaps. In an image subtraction test, VNN2 and DW reliably reconstructed images even if large amounts of data were missing. However, the quality of the reconstruction improved, if data acquisition was performed in a structured manner. When evaluating the diagnostic value of reconstructed axial, sagittal and coronal views, VNN2 and DW were judged to be significantly better than MPR and VNN.

Conclusion VNN2 and DW could be identified as robust algorithms that generate reconstructed US images with a high diagnostic value. These algorithms improve the utility and reliability of 3D-US imaging during intraoperative navigation. Copyright © 2012 John Wiley & Sons, Ltd.

Keywords three-dimensional ultrasound; intraoperative imaging; neurosurgery; reconstruction algorithms

Introduction

Neuronavigation systems have become a standard tool in neurosurgery. However, image guidance depending on preoperative images may become

Accepted: 23 December 2011

inaccurate due to brain shift during ongoing surgery (1–4). An update of the anatomy is needed using intraoperative imaging. While intraoperative magnetic resonance imaging (MRI) can be considered as the gold standard (5–8), it is time-consuming, expensive and demands special equipment and is therefore not ubiquitarily available. Intraoperative ultrasound (US) has been used in neurosurgical procedures since the early 1980s (9–11), as it is basically everywhere accessible and allows cheap, real-time imaging.

However, there are some major disadvantages using two-dimensional (2D) US: the limited insonation window of the cranial opening only allows certain planes of view, usually in an oblique orientation. This makes orientation more difficult for the neurosurgeon who is used to axial, coronal and sagittal imaging (12). Moreover the quality of the 2D images as well as their interpretation depend on the experience and skill of the examiner (13). Fenster *et al.* (13) also state that there might be difficulties in finding the exact view again when monitoring therapeutic procedures. In the neurosurgical setting, it can be difficult to compare 2D US during ongoing surgery to monitor the extent of a tumour resection.

Three-dimensional (3D) US addresses some of these problems by allowing advanced 3D analysis such as reslicing, surface and volume rendering, that once were exclusive to MRI and CT (14). In neurosurgery, a sensor-based freehand technique is usually used for 3D US acquisition (15–20). In summary, a position sensor is attached to the transducer and the relative location of the B-mode image to the sensor is determined through a probe calibration. The calibrated probe allows to measure position and orientation of the acquired images. During image acquisition, a set of 2D B-scans with the corresponding spatial information is acquired. These scans are usually distributed in a non-parallel manner over the area of interest. Reconstructing these images into a regular array allows 3D-visualization. An anyplane reslicing permits viewing the data in axial, coronal and sagittal image planes similar to MRI, thus improving orientation (21). Moreover, this might lead to a better comparison of pre- and post-resection images, possibly improving resection control in tumour surgery (22).

Due to the technical advances in 3D US, this imaging modality is used more frequently intraoperatively. However, further improvements are still necessary. The quality of 3D US depends on 2D image quality, a precise spatial registration and the reconstruction algorithm. Image reconstruction refers to the process of generating a 3D representation of the anatomy by placing the acquired 2D images in their correct relative positions and orientations in the 3D image volume and then using their pixel values to determine the voxel values in the 3D image (13). The examiner controls the motion of the probe in freehand 3D ultrasound acquisition, thus the distance and the orientation of the scans to each other are non-uniformly distributed. This means that

the positions of the pixels within a voxel array are irregular leading to a reconstruction problem that has been described as scattered (or unstructured) data interpolation (23). Advantages and disadvantages of different algorithms have been reviewed in controlled conditions elsewhere (24,25).

In this paper, we will focus on the reconstruction step in clinical data sets, as an unsuitable reconstruction algorithm might lead to a loss of image quality compared with 2D imaging. Moreover, artefacts due to the 3D reconstruction could possibly mislead the surgeon. The aim of the study is to compare different reconstruction algorithms with respect to image guidance in neurosurgery. Due to the sparsity of data the reconstruction algorithm must have a high interpolation capability. Moreover, a fast algorithm is required for surgical applications, as near real-time imaging is essential in this situation. Therefore, we tested algorithms with a relatively low computational complexity. Reconstructed images should have a high diagnostic value for the surgeon, because therapeutic decisions might be made according to these images.

Materials and methods

Patient data

Anonymized image data from seven patients, who underwent image guided resection of an intracerebral lesion using intraoperative sensor-based freehand 3D US between 2006 and 2008 at Marburg University Hospital, were selected retrospectively for the study from our library of 3D US data sets. Patients had given informed consent for intraoperative 3D US acquisition, image data collection and further studies. Selection criteria were low number of artefacts in the original 2D US images and a relatively dense 3D data volume with little gaps because we considered this to be essential for the evaluation of reconstruction algorithms.

There were five male and two female patients with a mean age of 46.6 years (21–77 years). Pathology included three glioblastomas, one anaplastic astrocytoma, two metastases and one hamartoma. The lesions were located in the frontal lobe in two cases, in the temporal lobe in two cases, in the parietal lobe in one case, intraventricularly in one case and in the cerebellum in one case, respectively.

Navigation and intraoperative three-dimensional ultrasound acquisition

The day before the operation, MRI for conventional intraoperative navigation was performed following the navigation protocol including T1 weighted images without contrast enhancement, T2, FLAIR and thin sliced (1 mm) T1 weighted images with contrast enhancement.

Magnetic resonance images (MRIs) were then transferred to the navigation station. An integrated ultrasound-navigation device with a laptop based ultrasound system (IGSonic, Brainlab, Feldkirchen, Germany) connected to a navigation system (VectorVision², Brainlab, Feldkirchen, Germany) as described previously (26) was used for intraoperative image acquisition and navigation (Figure 1 (a)–(c)). The navigation system consists of an optical tracking system using a stereo-infrared camera and reflective spheres. Precalibration of the ultrasound probe with a position sensor adapter with reflective spheres was performed prior to surgery using a calibration phantom as described previously (27). After induction of general anaesthesia, the patient's head was fixed in the Mayfield clamp and a reference star for navigation was mounted onto the Mayfield clamp. Patient registration was done using skin fiducials. A navigated craniotomy centred over the intracerebral lesion was carried out. After the craniotomy the precalibrated position sensor adapter was mounted on the sterile draped ultrasound probe (phased array, 5–9 MHz) that could be tracked by the infrared camera of the navigation station. There is only one way to mount the position sensor adapter onto the probe due to a special design of the adapter; therefore a new calibration prior to the intraoperative use was not necessary. A transdural ultrasound scan was performed manually. 256 2D US scans and their encoded positional information were stored by the navigation system per data set and reconstructed to a 3D volume (Figure 1(d)). The ultrasound data was then displayed in an axial, sagittal and coronal view with the corresponding MRIs side by side (Figure 1(e)).

Postoperative data processing

Postoperatively, MRIs and US images with the corresponding positional information were transferred to a regular computer and stored in an image library for post-hoc evaluation.

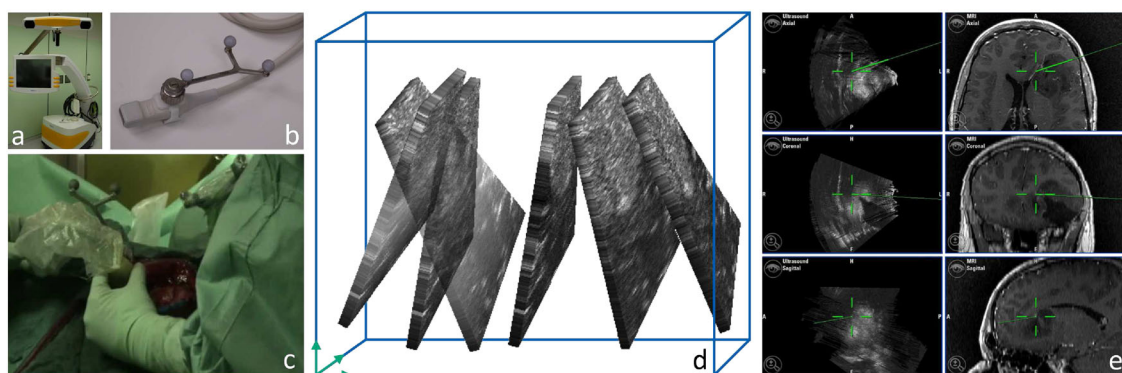


Figure 1. Navigated freehand 3D-ultrasound. (a, b) Navigation station with integrated US probe. Note the adapter for collecting spatial information mounted onto the ultrasound probe in image 1(b). (c) Acquisition of a 3D-US volume using a tracked freehand method. (d) Reconstruction of the 2D-US slices into a 3D-volume. (e) Reconstructed axial, coronal and sagittal US-images side by side with the corresponding MRIs in a recurrent left frontal low grade glioma. The green line represents the position of the tip of a pointer after tumour resection

The original patient data was imported into the programme Alcathon1.1 (Brainlab, Feldkirchen, Germany), which was designed to allow a visual comparison of different reconstruction algorithms. All individual patient information was anonymized. Five different reconstruction algorithms, a standard multiplanar reconstruction with interpolation (MPR), a pixel nearest neighbour method (PNN) (28), a conventional voxel nearest neighbour interpolation method (VNN) (25) and two different voxel based algorithms with distance weighted input (DW (29) and VNN2) were then performed. VNN2 is similar to the algorithm described by Barry *et al.* (14), however Barry described it as a pixel based algorithm whereas the algorithm here is voxel based. A short description of the algorithms is given in Table 1.

Evaluation

Image quality

After importing the patients' data sets into the Alcathon programme (see above), ten points P_i (with $i = 1, \dots, 10$) with the coordinates ($x/y/z$) were selected randomly in each data volume (Figure 2). The data was reconstructed using each single reconstruction algorithm described above. Slice thickness (MPR) and kernel size (VNN, VNN2, DW) were set to 1 mm, the gapfill radius (PNN) was set to 1 pixel for the primary reconstruction process and the evaluation of gap filling capacity described below.

Axial, sagittal and coronal images defined through point P_i were viewed; image quality and possible artefacts were noted. Moreover image quality and possible artefacts were described (1) after altering the parameters slice thickness, kernel size and gapfill radius for the different algorithms, (2) after creating artificial gaps as described below.

Gap filling capacity

In a second step, we tested the robustness of the algorithms to fill gaps within the sample volume. We therefore removed various amounts of input data from the data sets

Table 1. Reconstruction algorithms

Algorithm	Description
MPR	Standard multi-planar reconstruction Reconstructs an arbitrary orientated plane (e.g. axial, sagittal and coronal view-planes) out of any given (non-)orthogonal data set. The ultrasound 3D data consists of single images. Assuming a given slice thickness (parameter) the data set consist of a set of thick slices located in a 3D volume. A reconstruction plane is defined; the plane cutting through the data volume cuts the slices creating a polygonal border for every slice in the reconstruction plane. The resulting image is created by putting the pixels from the corresponding images into the polygon using tri-linear interpolation of neighbouring pixels. Parameter: <i>Slice thickness</i>
PNN	Pixel nearest neighbour reconstruction First, the algorithm loops over every pixel in every US-slice and puts every pixel in the nearest voxel of the target volume. If more than one pixel are to be put into the same target voxel, the arithmetic average of the values is used. In a second step, the algorithm loops over the target volume and fills the gaps. For every empty voxel, neighbouring voxels in a certain gap-fill radius (starting with a radius of 1 voxel) around the empty one are checked and averaged into one resulting value. If there are no filled voxels within the radius of 1 voxel, the radius is extended to 3 voxels, then to 5 voxels, if needed. Parameter: <i>Gap-fill radius</i>
VNN	Voxel nearest neighbour method The algorithm loops over the target volume and searches for the closest image slice for every target voxel, taking the kernel size as maximum distance allowed. The grey value of the closest pixel inside this slice is taken as the value for the voxel. Only the grey value of the pixel with the smallest distance to the voxel is used; other pixels in the kernel size radius are ignored. Parameter: <i>Kernel size</i>
VNN2	Voxel nearest neighbour method using distance weighted averaging The algorithm loops over the target volume. For every target voxel, all image slices having a distance smaller than the given kernel size, are collected. The grey values of the closest pixels inside these slices are averaged. The average uses the inverse distance to the voxel center as a weight. Parameter: <i>Kernel size</i>
DW	Distance weighted method Similar like VNN2, but the voxel position is projected orthogonal onto the collected slices inside the kernel size. A bilinear interpolation is performed and used to average the grey values from the original slices. Parameter: <i>Kernel size</i>

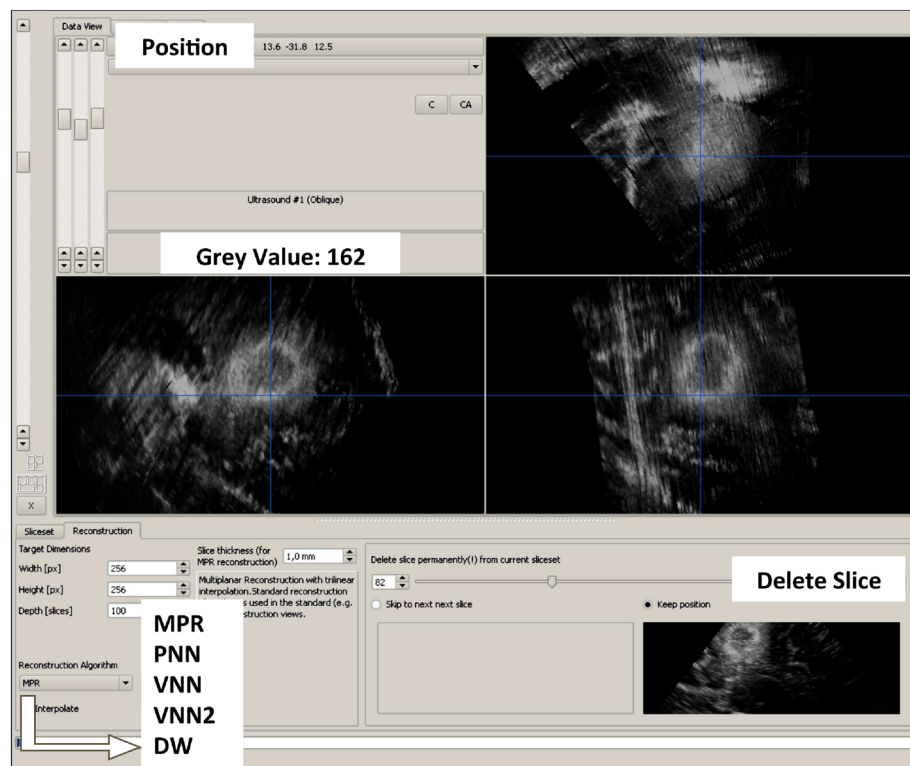


Figure 2. Evaluating image quality and the capability of the reconstruction algorithm to fill gaps. The data set of an occipital high grade glioma was displayed using the Alcatron programme. Reconstructed axial, sagittal and coronal views were shown and evaluated with regards to image quality and artefact formation. Points P_i (with $i = 1, \dots, 10$) within the data set were selected as indicated by the centre of the blue cross line. The coordinates ($x/y/z$) of the position of the point are displayed in the upper left corner of the image (in this example $x = 13.6/y = -31.8/z = 12.5$). The original grey value G_O of P_i as well as the grey value G_{R0} after application of the different algorithms was recorded. Then the 2D scan including P_i was deleted and another reconstruction was performed. The grey value G_{R-1} at position ($x/y/z$) was again noted.

and checked the algorithms' ability to recreate the removed data in a grey value analysis.

In a 2D US exam in B-mode the echo intensity of a given point is translated into brightness on a grey scale from zero to 255 (with 0 = black and 255 = white), which is visualized on an image. Every pixel on the B-mode scan therefore has a certain grey value G_O . As every US image in a 3D volume has corresponding positional information, we can define any point in the 3D volume with the coordinate ($x/y/z$) and the grey value G_O .

After the reconstruction process with the different algorithms the absolute grey value G_{R0} of the reconstructed image at point P_i was recorded. The difference ($G_{R0}-G_O$) between the reconstructed grey value G_{R0} and the original grey value G_O was noted. Then, the 2D US slice that included the point P_i was removed to form an artificial gap within the original data set. The reconstruction algorithm was performed and the grey value G_{R-1} at point P_i , as well as the difference ($G_{R-1}-G_O$) from the original grey value G_O was documented. Thereafter, the nearest 2D US slice to point P_i was again removed from the original data set. Again, a reconstruction was performed; the grey value G_{R-2} at point P_i and the difference ($G_{R-2}-G_O$) from the original grey value at this point were recorded. In total ten 2D US slices were removed that were closest to P_i in order to increase the size of the artificial gap within the data set. In each case this procedure was done in ten different positions P_i of the data set. Again axial, sagittal and coronal images defined through point P_i were viewed; image quality and possible artefacts were noted.

Data acquisition

We selected three patient data sets that showed a clear difference in the way of image acquisition to test the influence of different ways of data acquisition on the algorithm's ability to fill gaps. In visualizing the acquired original US slices, we could show that the transducer had been moved in a fan-like manner over the area of interest in patient 1. In patient 2, the US probe had been moved in a parallel manner, and in patient 3, the examiner had performed several sweeps from different insonation angles. The image pattern was similar in all three patients showing a cystic tumour. The data sets were imported into the Alcathon software. Slice thickness (MPR) and kernel size (VNN, VNN2, DW) were set to 1 mm, the gapfill radius (PNN) was set to 1 pixel. A plane x was randomly selected in the patient data set, that would cut all 2D slices. Twenty points Q_j (with $j = 1, \dots, 20$) were randomly selected in the plane x . The plane x was reconstructed with every algorithm to create the image I_{R0} (Figure 3(a)). Then, 20 2D US scans defined through the points Q_j were deleted. Again the image plane x was reconstructed with every algorithm to create image I_{R-20} (Figure 3(b)). This procedure was repeated for another 20 scans nearest to points Q_j until 100 scans were deleted. Each pixel in I_{R-20} to $R-100$ was subtracted from the corresponding pixel in I_{R0} . The absolute difference was displayed as a subtraction image

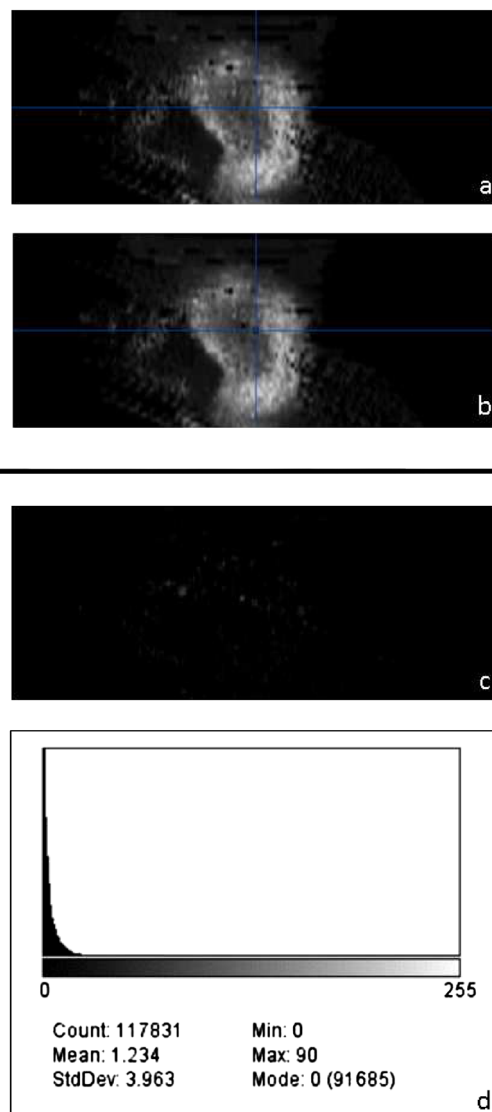


Figure 3. Image subtraction. An example of the image subtraction process is illustrated. (a) 2D image reconstruction I_{R0} in plane x using the full data set. (b) 2D image reconstruction I_{R-20} in the same plane of view using a data set from which 20 2D slices were deleted. Please note, that there are a few gaps in the centre of the image, where data is missing. (c) Subtraction result of the two images above. (d) The histogram displays the distribution of the pixel values in 3(c). Most pixels were black (0 on the grey scale), the brightest pixels showed a dark grey (90 on the grey scale) with a mean value of 1.234 ± 3.963 (standard deviation)

(Figure 3(c)). Results of the distribution of grey values in the subtraction image were displayed in a histogram (Figure 3(d)). The mean pixel values were calculated with standard deviations. Mean pixel values of the subtraction images and standard deviations were compared. A high mean pixel value signifies that pixels in I_{R-20} differ from pixels in I_{R0} . A greater standard deviation signifies a greater spread in pixel brightness.

Clinical evaluation

A total of 450 axial, coronal and sagittal reconstructed images in five different patient data sets were evaluated with respect to image quality by two different

neurosurgeons that were blinded towards the reconstruction algorithm. We selected data sets that included several anatomical landmarks such as ventricles, falx or other dural structures for the evaluation process. The ability to define tumour borders, to delineate ventricles and to depict dural structures in each image as well as an overall impression of the image were evaluated. A grade from 1 to 6 was given for each of the above-mentioned criteria with 1 = very good, 2 = good, 3 = satisfactory, 4 = fair, 5 = poor and 6 = completely unsatisfactory. An overall grade was calculated as the sum of the individual grades described above.

Afterwards, the two best algorithms were compared with the original 2D ultrasound images in all patient data sets in the US plane of view to check for artefact formation within the image.

Statistical analysis

A multifactorial variance analysis was used in grey value analysis to evaluate the gap filling capacity of the reconstruction algorithm. Results in the image subtraction exam to demonstrate the influence of data acquisition on

the reconstruction result were displayed in a descriptive manner. In the clinical evaluation, an ANOVA-model was used to evaluate the influence of the algorithm on the overall grade, taking the effect of the examiner into account.

Results

Evaluation

Image quality and artefact formation

MPR

With the slice thickness set to 1 mm the algorithm still left small gaps within the data volume (Figure 4(a), 5(a), green arrows). A reduction in slice thickness led to an increase in gap formation, so that anatomical structures were barely recognizable. Gaps were closed when the slice thickness was set to 1.5 mm and more. This led to a broadening at the image boundaries, but image quality remained unchanged compared with a slice thickness of 1 mm. Misalignment artefacts were obvious in all images (Figure 4(a), yellow arrow).

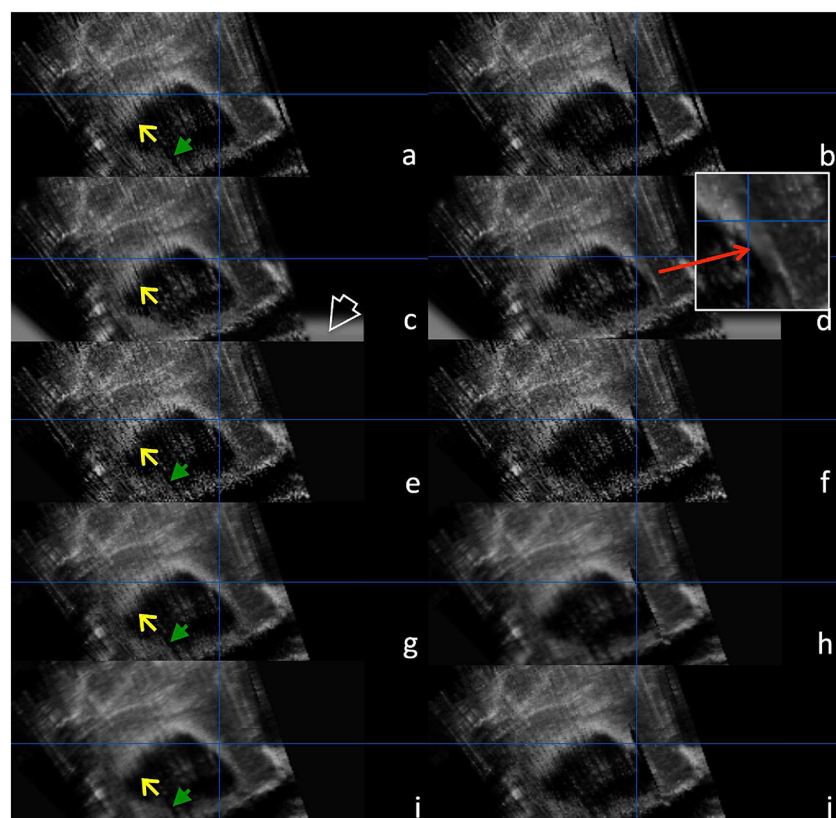


Figure 4. Image quality and gap filling capacity. Two reconstructed images from the data set of a patient with a cerebellar metastasis were used to illustrate image quality and gap filling capacity. The left column (a, c, e, g, i) represents the reconstruction R_0 , the right column (b, d, f, h, j) represents the reconstruction R_{-10} as described in the methods section. Ten scans were deleted in the area of the blue cross hairs. (a-b) MPR, (c-d) PNN, (e-f) VNN, (g-h) VNN2, (i-j) DW. Note the gap formation in R_{-10} . The reconstruction process of PNN by filling missing data leads to a blurry artefact, as shown in (d). The area of artefact formation is magnified. The same artefact occurs at the borders of the image (open white arrow). The green arrows indicate gaps that were not filled by the reconstruction algorithm in the first place. Note the slight misalignment artefacts that occur in all reconstruction algorithms (yellow arrows)

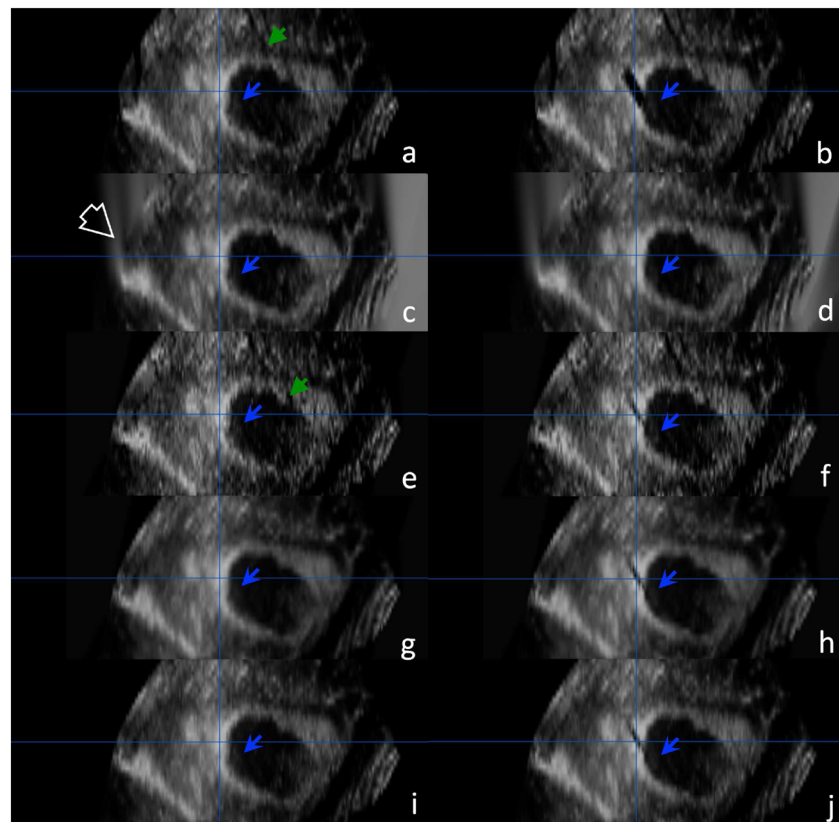


Figure 5. Image quality and gap filling capacity. Two reconstructed images from the data set of a patient with a cerebellar metastasis were used to illustrate image quality and gap filling capacity. The left column (a, c, e, g, i) represents the reconstruction R_0 , the right column (b, d, f, h, j) represents the reconstruction R_{-10} as described in the methods section. Ten scans were deleted in the area of the blue cross hairs. (a-b) MPR, (c-d) PNN, (e-f) VNN, (g-h) VNN2, (i-j) DW. Note the gap formation in R_{-10} . The reconstruction process of PNN by filling missing data leads to a blurry artefact, especially at the borders of the image (open white arrow). The green arrows indicate gaps that were not filled by the reconstruction algorithm in the first place. The blue arrows point to a rather fine structure that is visualized more or less clearly depending on the reconstruction algorithm and the gap formation

Gaps within the image enlarged with an increasing number of scans removed (Figure 4(b), 5(b)); two to three scans could be removed until a significant gap disturbed the image. Gaps were generally larger than in other reconstruction algorithms.

PNN

With the gapfill radius set to 1 pixel, the algorithm was very good at interpolation and filled almost all gaps within the data volume. However it also created white artefacts around the image that appeared like a smear (Figure 4(c), 5(c), white open arrow). Depending on the density of data a blurring occurred in some areas within the image, in others the image appeared more structured (Figure 4(d), magnification). If the gapfill radius was set to 0, there were obvious gaps within the image. They were closed if the gapfill radius was set to 1. An increase in gapfill radius did not change the image quality, as filled voxels were not changed, however, the smear artefact increased with increasing gapfill radius. Again there were misalignment artefacts visible (Figure 4(c), yellow arrow).

Although the algorithm did not show any gaps, fine structures might have disappeared due to the averaging of data. Interestingly, in Figure 5(c) fine structures (blue

arrow) were not visible, but reappeared after removal of data (Figure 5(d), blue arrow).

VNN

The algorithm left rather obvious gaps when the kernel size was set to 1 mm (Figure 4(e), 5(e), green arrows). Overall the image had more of a speckle appearance than the other reconstructions. Misalignment artefacts seemed to be more obvious than in PNN (Figure 4(e), yellow arrow). A reduction of the kernel size left more gaps unfilled, after an increase of the kernel size to 1.5 mm almost all gaps were filled. No other change in image quality could be noted. The algorithm always searches for the nearest pixel within the kernel size to fill the voxel. If the voxel is filled, it will not be changed again. Therefore a change in kernel size should not change image quality.

Gaps enlarged with an increasing number of scans removed (Figures 4(f), 5(f)); however, seven to eight scans could be removed until a significant gap disturbed the image. Even though gaps appeared, some of the fine structures were still visible (Figure 5(f), blue arrow).

VNN2

The algorithm left very small gaps, when the kernel size was set to 1 mm (Figure 4(g), green arrow). Images

appeared smoothed out. A slight misalignment artefact was visible, but it was not as disturbing as in VNN because of the smoothing (Figure 4(g), yellow arrow). A reduction of the kernel size left more gaps unfilled. If the kernel size increased above 1 mm all gaps were filled, a further increase of kernel size led to a decrease in image quality as it became more and more washed-out. Structures such as the falx became broadened. The reason is that the algorithm forms a distance-weighted average of all input values within the kernel size. With increasing kernel size more and more pixels are averaged.

Gaps enlarged with increasing number of scans removed (Figure 4 h, 5 h); four to five scans could be removed until a significant gap disturbed the image. Fine structures were well visible but were not completely reconstructed when data was removed (Figure 5(g), 5(h), blue arrows).

DW

The algorithm left very small gaps, when the kernel size was set to 1 mm (Figure 4(i), green arrow). Again misalignment artefacts were not as disturbing as in VNN due to the smoothening process (Figure 4(i), yellow arrow). A reduction of kernel size led to more gap formation. Above 1 mm kernel size all gaps were closed. A further increase in kernel size led to a smoothing of the images, however, a broadening of structures as in VNN2 could not be noticed.

Gaps enlarged with increasing number of scans removed (Figures 4(j), 5(j)); six or seven scans could be removed until a significant gap disturbed the image. Again there was a very smooth appearance of the image. Fine structures were well visible throughout the reconstructions (Figure 5(i), 5(j), blue arrows).

Gap filling capacity

All results are reported as difference on a grey scale (with 0 = black and 255 = white) with confidence intervals, results are displayed in Figure 6.

Number of deleted 2D scans	p-value (F-test)
0	0.7209
1	0.4375
2	0.0450
3	0.0218
4	0.0030
5	0.0013
6	0.0004
7	0.0028
8	<.0001
9	0.0004
10	<.0001

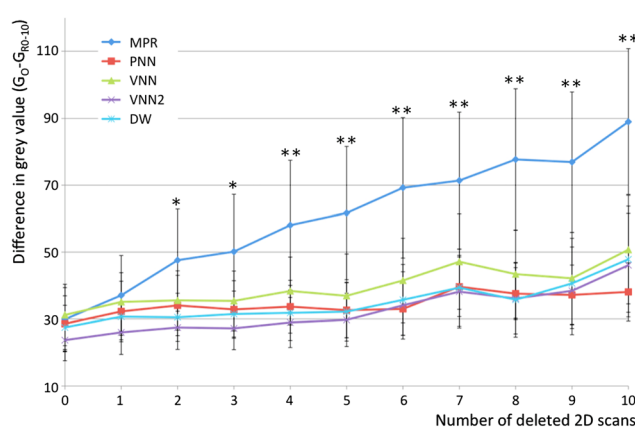


Figure 6. Gap filling capacity. Mean differences between the original grey value and the grey value in the reconstructed image are shown with confidence intervals. The original US-dataset included 256 2D slices. Up to 10 slices were deleted to test the robustness of the algorithm to fill gaps within the sample volume. Results of the different algorithms were compared using the F-test. P-values are given in the table, showing that MPR was significantly worse in image reconstruction when two US slices or more were deleted. There was no significant difference between any of the other reconstruction methods. *Significant; **highly significant

analysis, as MPR had the least capability of closing gaps. Results are summarized in Figure 7.

Clinical evaluation

When evaluating the diagnostic value of 450 reconstructed axial, sagittal and coronal images (Figure 8), VNN2 and DW were judged to be significantly better than MPR and VNN in the ANOVA model. Mean grades (standard errors) were 2.0 (0.12), 2.0 (0.13), 2.8 (0.24), 3.5 (0.25), respectively and 2.4 (0.18) for PNN (Figure 9).

No relevant artefact production was seen in VNN2 and DW when comparing the reconstructed images to the original 2D images. However, images appeared smoothed compared with the original 2D images.

Discussion

The value of 3D US has been recognized in many medical and surgical disciplines. Reconstruction of ultrasound data in 3D, allowing volumes to be measured independently of the data acquisition views, was reported as early as 1980 (32). However, it took another two decades until this technique was used in neurosurgery (15–20).

We believe that a basic understanding of the underlying technology is important for the surgeon to improve the value of this technique.

The quality of 3D US depends on 2D image quality, a precise spatial registration and the reconstruction algorithm. 2D image quality depends on the US probe as well

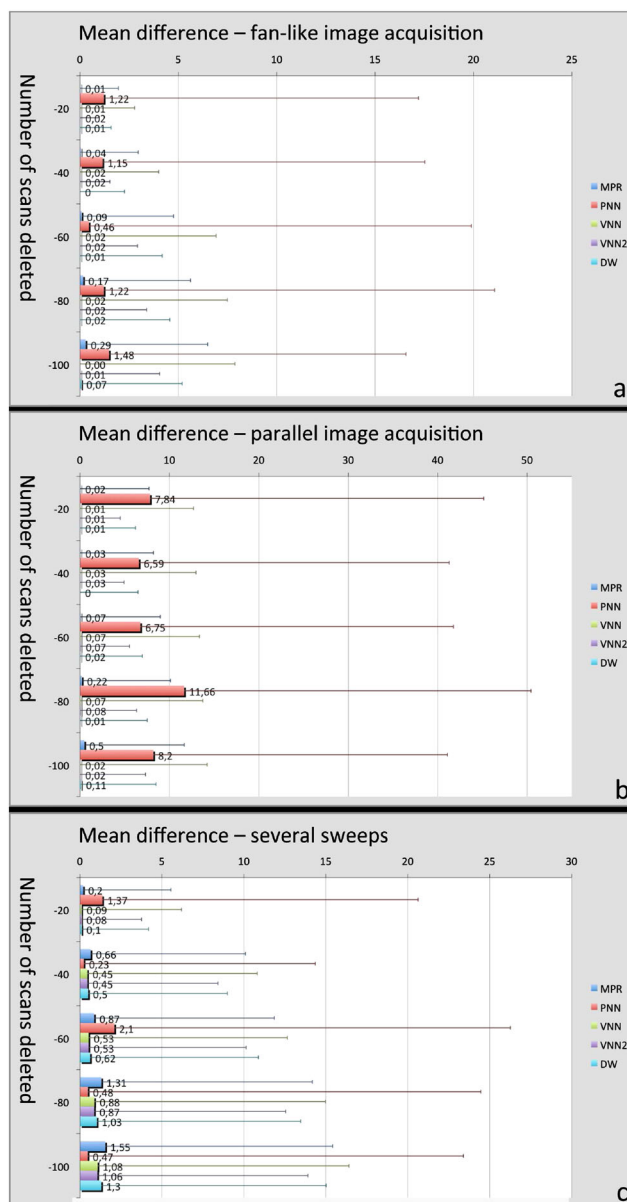


Figure 7. Image subtraction. (a) Fan-like image acquisition. (b) Parallel image acquisition. (c) Image acquisition using several US sweeps from different angles. Mean pixel values of the subtraction images (as displayed in Figure 3) with standard deviations are presented on the chart

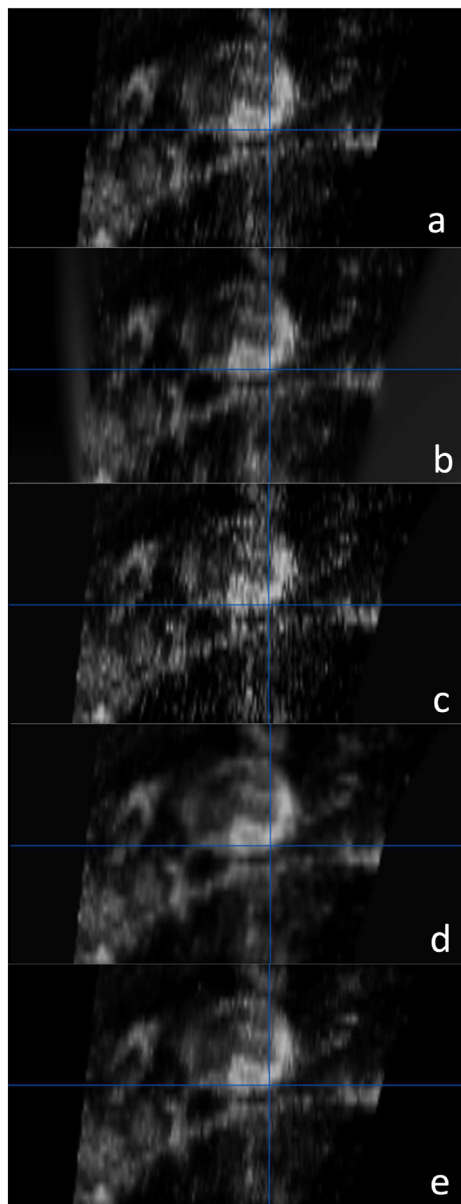


Figure 8. Evaluation of the diagnostic value of different reconstruction mechanisms. Example of one reconstructed image showing a temporomesial hamartoma. The tentorium is clearly visible, too. (a) MPR, (b) PNN, (c) VNN, (d) VNN2, (e) DWI

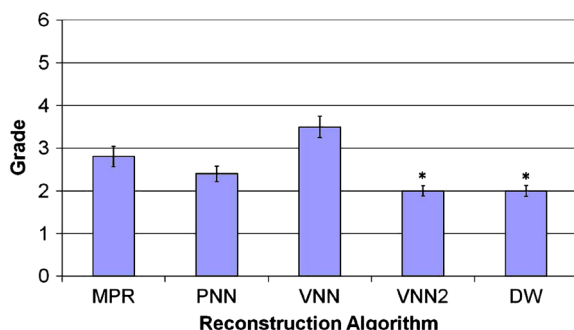


Figure 9. Evaluation of the diagnostic value of different reconstruction mechanisms. Mean grades for each algorithm are shown with standard deviations. *Significant

as the handling in theatre, so that artefacts can be reduced. A precise calibration of the probe is important, as reviewed by Mercier *et al.* (33). A basic understanding of the reconstruction algorithm is important already during image acquisition as many algorithms have difficulties in handling overlapping data (34). This is supported by our results using an image subtraction test. We could show that most reconstruction algorithms did better if the data was acquired in a parallel or fan-like sweep over the area of interest as compared to an unstructured manner. A fan-like data acquisition method seemed to lead to the best reconstruction results. However, this has to be confirmed in a bigger series.

Advantages and disadvantages of different reconstruction algorithms

MPR is a standard multi-planar reconstruction with trilinear interpolation for any-slice reconstruction that is designed for structured or isotropic data. Evaluation of gap filling capacity showed that MPR was significantly worse than the other reconstruction algorithms in filling bigger gaps. Moreover, its diagnostic value in the clinical evaluation was judged to be inferior to VNN2 and DW. We therefore judged MPR as unsuitable for 3D US reconstruction in the neurosurgical setting.

There are a number of reviews on different algorithms specially designed for 3D US reconstruction. Rohling *et al.*, (24) grouped algorithms according to how they worked in PNN, VNN and distance weighted algorithms, whereas Solberg *et al.*, (25) sorted algorithms on how they were implemented in pixel based, voxel based or function based algorithms. Even though the grouping by Solberg *et al.* allows a better understanding of the implementation, the function and weight of the local neighbourhood used for data input seem to be more important in clinical practice. We therefore preferred to group the algorithms used in our setting in PNN, VNN and two distance-weighted algorithms VNN2 and DW.

The pixel nearest neighbour (PNN) algorithm has been described by McCann *et al.* (30), Hottier and Billon (31), Nelson and Pretorius (28), and others. The PNN is a two-stage algorithm with a so-called bin-filling or distribution step and a hole-filling step. First, the algorithm traverses every pixel in every US-slice and distributes the input data to the nearest voxel (bin-filling step). Parameters to be set are the weights of multiple contributions to the same voxel. In this second step, the algorithm loops over the target volume and fills the gaps. The parameters to be set here are the weights of the contributing voxels.

In our setting, pixels were averaged if more than one pixel were placed into the same target voxel. Gaps that occurred, if the scanning interval was larger than the voxel size, were filled by averaging the value of voxels in a certain radius around the empty voxel.

We could show that voxels filled in the second step of the reconstruction algorithm had a smoothed appearance

compared with voxels filled in the first step. Moreover, a strong artefact formation could be noted at the borders of the image. Both effects probably led to high mean pixel values and high standard deviation in subtraction images. We can therefore conclude that even though the algorithm tried to fill gaps, brightness seemed to differ in the reconstructed image. This might even mislead the surgeon in certain cases during image-guided surgery. We therefore judged PNN as less suitable than VNN2 and DW in the neurosurgical setting.

In VNN the algorithm traverses each voxel and fills it with the value of the nearest pixel (35). This is a very fast method, but is prone to artefacts due to registration errors such as motion artefacts and sensor errors (24). In our setting, the greatest pixel value was taken, if there were several input pixels with the same distance. Although the algorithm showed good performance in the image subtraction test, the diagnostic value of the technique was judged to be inferior to the distance-weighted methods. The algorithm was graded badly in the clinical evaluation, most likely due to the rather obvious speckle pattern and the motion artefacts that reduced the capability of delineating anatomical structures. Due to the lack of diagnostic value, VNN was judged to be less suitable than VNN2 and DW in the neurosurgical setting.

Distance-weighted methods can be pixel-based interpolations (14,36,37) or voxel based interpolations (29,38). The distance to the voxel weights the input data in a local neighbourhood of the voxel. Parameters to be set are the weight function and the size and shape of the local neighbourhood. In VNN2 a spherical kernel and an inverse distance weight were employed. If kernel size was set too small, gaps occurred. If kernel size was too large, the voxel array appeared too smoothed. In DW a bilinear interpolation according to Trobaugh *et al.* (38) was applied. The voxel position was projected orthogonal onto the nearest slices and the grey value was interpolated from the surrounding pixels in a distance-weighted manner. This method had the advantage of retaining the resolution of each B-scan in the voxel array and avoided gaps. However, in cases of nonlinear sweeps, it might be difficult to choose the nearest slices. Both algorithms showed the best overall performance in gap filling capabilities and in clinical evaluation. VNN2 and DW were judged to be significantly better in diagnostic imaging than MPR and VNN. Both VNN2 and DW had a smoother appearance making it easier for the clinician to recognize certain structures. Both algorithms were therefore judged to be good candidates to be implemented in a neurosurgical setting.

There are several algorithms described in the literature that estimate a function of the input data to create a voxel grid such as a Rayleigh interpolation with Bayesian framework (39) and a radial basis function interpolation (24). As these algorithms are more demanding on computational time, we did not consider them as suitable algorithms for an intraoperative setting and therefore did not test these algorithms.

Impact of data acquisition on the reconstruction result

Most algorithms except PNN performed better, when image data was acquired in a rather structured way such as a parallel or fan-like US sweep. These findings are conclusive with the work of Huang *et al.* (34). Even though a compounding of data by acquiring data from different insonation angles may reduce speckle noise and registration errors (14,34), handling of overlapping data seems to be problematic for most algorithms and results in a reduced spatial resolution due to averaging (34). A reduced spatial resolution will eventually reduce the diagnostic value of the reconstructed image. Solutions that have been discussed in the literature by different authors such as 'super resolution image reconstruction' techniques (34,36) might still use too much computational time for intraoperative use.

For the clinician it is therefore important to know the reconstruction algorithm that is applied to acquire data in the way that is best for 3D reconstruction.

Limitations of the study

This is a retrospective data analysis of selected patient data sets. Using surgical patient data sets best represents the real situation in a neurosurgical operating theatre. However, these data sets might contain more artefacts than data sets of phantoms or volunteers as described by other authors, previously (24,29,40). We evaluated the impact of the way of data acquisition on the reconstruction result by an image subtraction method, as this is a very good way of comparing images. However, a statistical analysis of these data is difficult to achieve. We could demonstrate that a structured data acquisition led to a better reconstruction result in the selected cases. However, these results need to be further evaluated in a prospective study.

Conclusion

VNN2 and DW were identified as robust algorithms that generate reconstructed US images with a high diagnostic value. These algorithms improve the utility and reliability of 3D-US imaging during intraoperative navigation. These algorithms are good candidates for an intraoperative evaluation in a larger patient cohort in a prospective manner. However, caution should be exercised during image acquisition to produce a rather structured data set to reach a high quality reconstruction.

Acknowledgement

The Department of Neurosurgery, University Clinic Essen, has a bilateral contract with Brainlab AG, Feldkirchen,

Germany, on the development and the evaluation of ultrasound-integration into neuronavigation. Brainlab owns part of the ultrasound equipment, all neuronavigation tools are owned by the Department of Neurosurgery. The programme Alcathon was provided by the company. F. Vollmer is employed by Brainlab, C. Lippert was employed by Brainlab during the data acquisition phase of the study. All other authors do not and did not receive any financial support from Brainlab.

References

- Hill DL, Maurer CR, Jr, Maciunas RJ, et al. Measurement of intraoperative brain surface deformation under a craniotomy. *Neurosurgery* 1998; **43**: 514–526.
- Nabavi A, Black PM, Gering DT, et al. Serial intraoperative magnetic resonance imaging of brain shift. *Neurosurgery* 2001; **48**: 787–797; discussion 797–788.
- Nimsky C, Ganslandt O, Cerny S, et al. Quantification of, visualization of, and compensation for brain shift using intraoperative magnetic resonance imaging. *Neurosurgery* 2000; **47**: 1070–1079.
- Roberts DW, Hartov A, Kennedy FE, et al. Intraoperative brain shift and deformation: a quantitative analysis of cortical displacement in 28 cases. *Neurosurgery* 1998; **43**: 749–758.
- Albayrak B, Samdani AF, Black PM. Intra-operative magnetic resonance imaging in neurosurgery. *Acta Neurochir (Wien)* 2004; **146**: 543–556.
- Nimsky C, Ganslandt O, Von Keller B, et al. Intraoperative high-field-strength MR imaging: implementation and experience in 200 patients. *Radiology* 2004; **233**: 67–78.
- Schwartz RB, Hsu L, Wong TZ, et al. Intraoperative MR imaging guidance for intracranial neurosurgery: experience with the first 200 cases. *Radiology* 1999; **211**: 477–488.
- Wirtz CR, Bonsanto MM, Knauth M, et al. Intraoperative magnetic resonance imaging to update interactive navigation in neurosurgery: method and preliminary experience. *Comput Aided Surg* 1997; **2**: 172–179.
- Chandler WF, Knaake JE, McGillicuddy JE, et al. Intraoperative use of real-time ultrasonography in neurosurgery. *J Neurosurg* 1982; **57**: 157–163.
- Masuzawa H, Kamitani H, Sato J, et al. Intraoperative application of sector scanning electronic ultrasound in neurosurgery (author's transl). *Neurol Med Chir (Tokyo)* 1981; **21**: 277–285.
- Rubin JM, Mirfakhraee M, Duda EE, et al. Intraoperative ultrasound examination of the brain. *Radiology* 1980; **137**: 831–832.
- Miller D, Heinze S, Tirakotai W, et al. Is the image guidance of ultrasonography beneficial for neurosurgical routine? *Surg Neurol* 2007; **67**: 579–587.
- Fenster A, Downey DB, Cardinal HN. Three-dimensional ultrasound imaging. *Phys Med Biol* 2001; **46**: R67–99.
- Barry CD, Allott CP, John NW, et al. Three-dimensional freehand ultrasound: image reconstruction and volume analysis. *Ultrasound Med Biol* 1997; **23**: 1209–1224.
- Bonsanto MM, Staibert A, Wirtz CR, et al. Initial experience with an ultrasound-integrated single-RACK neuronavigation system. *Acta Neurochir (Wien.)* 2001; **143**: 1127–1132.
- Gronningsaeter A, Kleven A, Ommedal S, et al. SonoWand, an ultrasound-based neuronavigation system. *Neurosurgery* 2000; **47**: 1373–1379.
- Pennec X, Cachier P, Ayache N. Tracking brain deformations in time-sequences of 3D US images. *Pattern Recog Lett* 2003; **24**: 801–813.
- Trantakis C, Meixensberger J, Lindner D, et al. Iterative neuro-navigation using 3D ultrasound. A feasibility study. *Neurol Res* 2002; **24**: 666–670.
- Tronnier V, Bonsanto MM, Staibert A, et al. Comparison of intraoperative MR imaging and 3D-navigated ultrasonography in the detection and resection control of lesions. *Neurosurg Focus* 2001; **10**: 1–5.
- Unsgaard G, Ommedal S, Muller T, et al. Neuronavigation by intraoperative three-dimensional ultrasound: initial experience during brain tumor resection. *Neurosurgery* 2002; **50**: 804–812.
- Bozinov O, Burkhardt JK, Fischer CM, et al. Advantages and limitations of intraoperative 3D ultrasound in neurosurgery. Technical note. *Acta Neurochir Suppl* 2011; **109**: 191–196.
- Rohde V, Coenen VA. Intraoperative 3-dimensional ultrasound for resection control during brain tumour removal: preliminary results of a prospective randomized study. *Acta Neurochir Suppl* 2011; **109**: 187–190.
- Nelson TR, Pretorius DH. Three-dimensional ultrasound imaging. *Ultrasound Med Biol* 1998; **24**: 1243–1270.
- Rohling R, Gee A, Berman L. A comparison of freehand three-dimensional ultrasound reconstruction techniques. *Med Image Anal* 1999; **3**: 339–359.
- Solberg OV, Lindseth F, Torp H, et al. Freehand 3D ultrasound reconstruction algorithms - a review. *Ultrasound Med Biol* 2007; **33**: 991–1009.
- Tirakotai W, Miller D, Heinze S, et al. A novel platform for image-guided ultrasound. *Neurosurgery* 2006; **58**: 710–718.
- Vince GH, Krone A, Woydt M, Roosen K. Real time ultrasound fusion in optical tracking MRT/CT image guided surgery. In *Proceedings of the XIII Congress of the European Society for Stereotactic and Functional Neurosurgery*. 1998; 1–5.
- Nelson TR, Pretorius DH. Interactive acquisition, analysis and visualization of sonographic volume data. *Int J Imaging Syst Technol* 1997; **8**: 26–37.
- Coupe P, Hellier P, Morandi X, Barillot C. Probe trajectory interpolation for 3D reconstruction of freehand ultrasound. *Med Image Anal* 2007; **11**: 604–615.
- McCann HA, Sharp JC, Kinter TM, McEwan CN, Barillot C, Greenleaf JF. Multidimensional ultrasonic imaging for cardiology. *Proc IEEE* 1988; **76**(9) 1063–1073.
- Hottier F, Billon AC. 3D echography: Status and perspective. In *3D Imaging in Medicine*, Hohne KH, Fuchs H, Pizer SM (eds). Springer-Verlag: Berlin, Heidelberg, 1990; 21–41.
- Moritz WE, Medema DK, Ainsworth M, et al. Three-dimensional reconstruction and volume calculation from a series of nonparallel, real-time, ultrasonic images. *Circulation* 1980; **62**(Suppl): 111–143.
- Mercier L, Lango T, Lindseth F, Collins LD. A review of calibration techniques for freehand 3-D ultrasound systems. *Ultrasound Med Biol* 2005; **31**: 143–165.
- Huang W, Zheng Y. MMSE reconstruction for 3D freehand ultrasound imaging. *Int J Biomed Imaging* 2008; **2008**: 274164.
- Sherebin S, Fenster A, Rankin RN, Spence D. Freehand three-dimensional ultrasound: implementation and applications. *Proc SPIE* 1996; **2708**: 296–303.
- Meairs S, Beyer J, Hennerici M. Reconstruction and visualization of irregularly sampled three- and four-dimensional ultrasound data for cerebrovascular applications. *Ultrasound Med Biol* 2000; **26**: 263–272.
- Ohbuchi R, Chen D, Fuchs H. Incremental volume reconstruction and rendering for 3D ultrasound imaging. Proc SPIE 1992; Vol. **1808**; Visualization in Biomedical Computing Richard A. Robb (Ed.); pp 312–323.
- Trobaugh JW, Trobaugh DJ, Richard WD. Three-dimensional imaging with stereotactic ultrasonography. *Comput Med Imaging Graph* 1994; **18**: 315–323.
- Sanches JM, Marques JS. A multiscale algorithm for three-dimensional free-hand ultrasound. *Ultrasound Med Biol* 2002; **28**: 1029–1040.
- Solberg OV, Lindseth F, Bo LE, et al. 3D ultrasound reconstruction algorithms from analog and digital data. *Ultrasonics* 2011; **51**: 405–419.